Weak lensing and spectroscopic analysis of the nearby dissociative merging galaxy cluster Abell 3376

R. Monteiro-Oliveira,[1,2]★ G. B. Lima Neto,[1] E. S. Cypriano,[1] R. E. G. Machado,[3] H. V. Capelato,[4] T. F. Laganá,[4] F. Durret[5] and J. Bagchi[6]

[1]*Instituto de Astronomia, Geofísica e Ciências Atmosféricas, Universidade de São Paulo, R. do Matão 1226, 05508-090 São Paulo, Brazil*
[2]*Departamento de Astronomia, Instituto de Física da Universidade Federal do Rio Grande do Sul, Campus do Vale, 91501-970 Porto Alegre, Brazil*
[3]*Departamento Acadêmico de Física, Universidade Tecnológica Federal do Paraná, Rua Sete de Setembro 3165, 80230-901 Curitiba, Brazil*
[4]*Núcleo de Astrofísica Teórica, Universidade Cruzeiro do Sul, Rua Galvão Bueno, 868, 01506-000 São Paulo, Brazil*
[5]*UPMC-CNRS, UMR 7095, Institut d'Astrophysique de Paris, F-75014 Paris, France*
[6]*The Inter-University Centre for Astronomy and Astrophysics (IUCAA), Post Bag 4, Pune 411007, India*

ABSTRACT

The galaxy cluster Abell 3376 is a nearby ($\bar{z} = 0.046$) dissociative merging cluster surrounded by two prominent radio relics and showing an X-ray comet-like morphology. The merger system is comprised of the subclusters A3376W and A3376E. Based on new deep multiwavelength large-field images and published redshifts, we bring new insights about the history of this merger. Despite the difficulty of applying the weak lensing technique at such low redshift, we successfully recovered the mass distribution in the cluster field. Moreover, with the application of a two-body model, we have addressed the dynamics of this merging system. We have found the individual masses of $M_{200}^{W} = 3.0^{+1.3}_{-1.7} \times 10^{14}$ M$_\odot$ and $M_{200}^{E} = 0.9^{+0.5}_{-0.8} \times 10^{14}$ M$_\odot$. The cometary-shaped X-ray distribution shows only one peak spatially coincident with both eastern BCG and the A3376E mass peak whereas the gas content of A3376W seems to be stripped out. Our data allowed us to confirm the existence of a third subcluster located at the north, 1147 ± 62 kpc apart from the neighbour subcluster A3376E and having a mass $M_{200}^{N} = 1.4^{+0.7}_{-1.0} \times 10^{14}$ M$_\odot$. From our dynamical analysis, we found the merging is taking place very close to the plane of the sky, with the merger axis just $10° \pm 11°$ from it. The application of a two-body analysis code showed that the merging cluster is seen $0.9^{+0.2}_{-0.3}$ Gyr after the pericentric passage and it is currently going to the point of maximum separation between the subclusters.

Key words: gravitational lensing: weak – galaxies: clusters: individual: Abell 3376 – dark matter – large-scale structure of Universe.

1 INTRODUCTION

Mergers of galaxy clusters are the central mechanism in the formation of the large-scale structure of the universe. According to the ΛCDM model, galaxy clusters live at the top of the halo mass-function, being formed through a continuous sequence of mergers of smaller structures (e.g. Feretti, Gioia & Giovannini 2002). These mergers are massive, with subcomponent masses of $\sim 10^{14}$ M$_\odot$ and occur at high relative velocities (~ 2000 km s^{-1}) and with small impact parameters. At around $\sim 10^{64}$ erg, they constitute the highest energy events since the big bang (Sarazin 2004). Many happen in directions along cosmic filaments, in which matter is distributed in the largest scales (Feretti et al. 2002).

As the only cluster component subjected to plasma physics during the merger, the intracluster medium (ICM) presents the most dramatic signatures of these events, in the form of shocks and cold fronts (Markevitch & Vikhlinin 2007). At least for a short period of time, hydrodynamical phenomena can displace the ICM distributions of subclusters relative to their dark matter haloes (DMH). This detachment can be partial (e.g. Monteiro-Oliveira et al. 2017) or even total (e.g. Clowe, Gonzalez & Markevitch 2004). Systems that show this feature are known as dissociative mergers (Dawson 2013).

These shocks induced on the ICM have, in general, Mach numbers $\mathcal{M} \lesssim 3$ (e.g. Akamatsu et al. 2012) and can (re)accelerate relativistic electrons that will emit diffuse, non-thermal synchrotron radiation in radio. These emissions can be then detected but they will not be associated with a single source (e.g. Feretti et al. 2002). They are the so-called radio relics, which are related to disturbed systems (e.g. Cassano et al. 2010), although they are not always present in merging clusters.

The galaxy cluster Abell 3376 (hereafter A3376) is a nearby ($\bar{z} = 0.046$; Struble & Rood 1999) merging system, as revealed
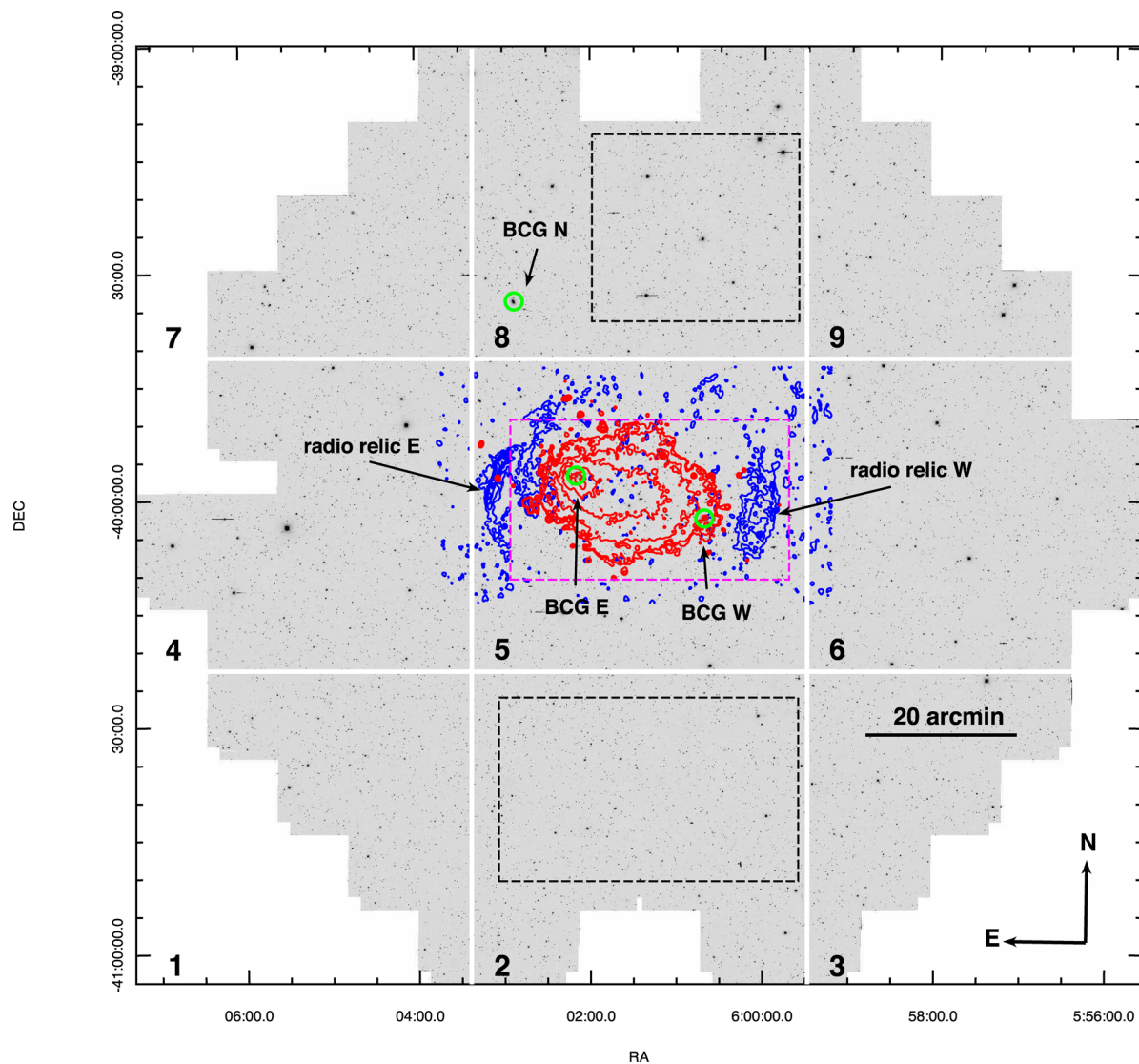
Figure 1. Optical r' image of A3376 obtained with the Blanco/DECAM imager. Overlaid are the X-ray emission contours as seen by the satellite *XMM–Newton* (red) and the radio emission mapped by the VLA telescopes (blue). The BCGs, including the northern candidate are marked by green circles. The cluster X-ray emission has a morphology similar to a comet whose main axis is nearly aligned with the segment along the BCGs W and E and the tail points towards the brightest one. In the outskirts, we have two diffuse radio emissions not associated with any single sources: the radio relics. As the image is large ($\sim$2.2 deg^2), it was divided into nine frames aiming for the weak lensing analysis. The dashed boxes show the regions considered for the statistical subtraction to identify the cluster red sequence galaxies: whereas these galaxies are supposed to prevail in the central magenta region, it is expected that their contribution diminish inside the black regions.

by its disturbed ICM (Ebeling et al. 1996; Flin & Krywult 2006) and the presence of two radio relics at the cluster outskirts (Bagchi et al. 2006; Kale et al. 2012; George et al. 2015). The X-ray surface brightness is very high, corresponding to an X-ray luminosity at the cluster redshift of $L_{X[0.5-2.0 \text{ keV}]} = 5.72 \times 10^{43}$ erg s^{-1} (Parekh et al. 2015) having a comet-like morphology, with its major axis closely aligned with the line connecting the two BCGs, as shown in Fig. 1. For this system, Akamatsu et al. (2012) obtained $\mathcal{M} = 2.91 \pm 0.91$ leading to a shock velocity upper limit $v_{\text{shock}} < 2000$ km s^{-1}, believed to have been generated 0.32 Gyr ago. These radio relics are separated by $\sim$2 Mpc and are nearly perpendicular to the line along the BCGs. Furthermore, George et al. (2015) argue that they are consistent with a shock propagation initiating $\sim$0.37 Gyr ago.

For its optical counterpart, Ramella et al. (2007) have found in the WIde-field Nearby Galaxy-cluster Survey (WINGS; Fasano

et al. 2006) two overdensities in the galaxy projected positions that match the location of BCGs. They have also reported mild evidence for a third galaxy concentration, but since it was very near the image border, more conclusions could not be drawn. In fact, there is a bright red galaxy located in that region, as revealed by our large field-of-view image. Moreover, Durret et al. (2013) have shown that the galaxy B-luminosity function is notoriously disturbed, as expected for post-merger systems. Examining redshift catalogues available in the literature, they found no clear bimodal scenario in the BCG region as pointed by Ramella et al. (2007).

Using N-body hydrodynamical simulations, Machado & Lima Neto (2013) had proposed a scenario of a post minor-merger (mass ratio around 1:6–1:8) whose pericentric passage would have happened 0.5 Gyr before the observed configuration. Due to the unavailability of lensing data at the time, those authors had considered the BCGs ($\sim$970 kpc apart from each other) as tracers of the DMH

centroids. Also due to the lack of lensing analysis, the total cluster mass was only known from the galaxies velocity dispersion ($M_{\rm vir} \approx 5 \times 10^{14}$ M$_\odot$; Girardi et al. 1998). The velocity dispersion, however, is known to be boosted in epochs close to pericentric passages (e.g. Pinkney et al. 1996; Monteiro-Oliveira et al. 2017), which can lead to mass overestimation.

In this context, this work presents the first weak lensing analysis of A3376. From deep r' images taken from the Dark Energy Camera (DECAM) mounted on the Blanco Telescope, we derived weak lensing masses. Using a redshift catalogue from literature, we have assigned member galaxies to their respective subclusters and performed their dynamical analysis. Subsequently, with both mass and dynamical information combined, we have addressed the merger scenario of A3376 assuming a two-body dynamical model (Dawson 2013). Finally, photometric and spectroscopic data allowed us to confirm the existence of a third subcluster, as previously suggested by Ramella et al. (2007), north of the already known merging system (see Fig. 1).

Although weak lensing has been thoroughly used to probe galaxy clusters, its application to low-redshift systems brings an additional challenge. The lensing signal is closely related to the (angular diameter) distance between the lens and background source galaxies, penalising clusters at very low redshifts (e.g. Spinelli et al. 2012).

This paper is organized as follows. In Section 2, we present the weak lensing analysis, from the description of the data up to the mass measurements. The dynamical overview based on the galaxy redshift analysis, can be found in Section 3. The proposed merger scenario for A3376 is described in Section 4. All results obtained are discussed in Section 5 and summarized in Section 6.

Throughout this paper, we adopt the following cosmology: $\Omega_{\rm m} = 0.27$, $\Omega_\Lambda = 0.73$, $\Omega_k = 0$, and $H_0 = 70$ km s^{-1} Mpc^{-1}. At the mean cluster redshift of $z = 0.0461$, we then have 1 arcsec equals 0.905 kpc, the age of the Universe 13.2 Gyr and an angular diameter distance of 186.4 Mpc.

2 WEAK LENSING ANALYSIS

2.1 A very quick review

Weak gravitational lensing is a powerful technique to recover mass distributions of galaxy clusters that works by measuring the distortion caused on the background galaxy shapes. Basically, the lens phenomenon in the weak regime[1] can be formalized as an isotropic convergence effect κ plus an anisotropic distortion described by the shear $\gamma = \gamma_1 + i\gamma_2$ where

$$\gamma_1 = |\gamma|\cos(2\theta), \quad \gamma_2 = |\gamma|\sin(2\theta) \tag{1}$$

and θ is the shear direction. Mathematically, both convergence and shear quantities are related to the second derivatives of the 2D-projected gravitational potential (e.g. Mellier 1999; Schneider 2005).

The convergence corresponds to the projected surface mass density of the lens,

$$\kappa = \frac{\Sigma}{\Sigma_{\rm cr}}, \tag{2}$$

where we define the lensing critical density as

$$\Sigma_{\rm cr} = \frac{c^2}{4\pi G}\frac{D_{\rm c}}{D_{\rm ds}D_{\rm d}}, \tag{3}$$

---

[1] The weak regime corresponds to $\kappa \ll 1$.

Band	Total exposure (h)	Seeing (arcsec)
g'	0.88	1.20
r'	1.66	1.20
i'	0.55	1.16

with $D_{\rm c}$, $D_{\rm ds}$ and $D_{\rm d}$ being the angular diameter distances to the source, between the lens and the source, and to the lens, respectively. The signal strength depends, then, on the distance between the lens and background objects. Together with the known distribution of galaxies that can be background sources for clusters ($\bar{z}_{\rm back} \approx 1$ per deep surveys; e.g. Coupon et al. 2009), it is expected that galaxy clusters located at intermediate redshifts ($z \sim 0.25$–0.50) are the most efficient deflectors (e.g. Spinelli et al. 2012), whereas nearby lenses (as A3376) will display a very low signal.

In the absence of a massive deflector in the foreground, a sample of distant galaxies will exhibit null average ellipticity, $\langle e \rangle \approx 0$. The effect of the lens is to induce on this sample a coherent ellipticity that corresponds to an effective shear g,

$$\langle e \rangle \simeq g \equiv \frac{\gamma}{1 - \kappa}, \tag{4}$$

represented by a spin-2 tensor (as well as γ and e). Normally, these quantities are defined in terms of its tangential component (in relation to the lens centre), g_+, and another one 45° in relation to that, $g_\times$.

2.2 Imaging data

Our imaging data were taken with the Dark Energy Camera (DECAM) of the Victor Blanco 4m-telescope (Proposal ID: 2013B-0627; PI: Gastão Lima Neto) within the SOAR Telescope time exchange program. Its large FoV (~ 2 deg^2) makes it suitable for lensing analysis of a close system, which is expected to cover a large area on the sky. Observational details are presented in Table 1. Before being delivered to the PI, the images were reduced and astrometrically calibrated by the telescope staff (Valdes, Gruendl & DES Project 2014).

Unlike other telescopes, Blanco allows only observations in the classical mode. Unfortunately, our science observations were made under non-photometric conditions, making it difficult to calibrate in the AB system from standard star fields (Adelman-McCarthy 2011) observed in the same night. We overcame this by using tabulated first-order extinction coefficients provided by the telescope staff (Alistair Walker, private communication).

Photometric catalogues were created with SExtractor (Bertin & Arnouts 1996) using the double mode detection based on the deepest r' band. Galaxies were selected with two complementary criteria: bright objects were considered galaxies if they had their CLASS_STAR index smaller than 0.8, whereas the faintest, $r' \geq 19$, galaxies had their full width half-maximum (FWHM) greater than 1.24 arcsec.

2.3 Finding the cluster member galaxies

As pointed by Dressler (1980), red elliptical galaxies are dominant in the inner region of galaxy clusters, acting as good tracers for these structures. Although cluster member galaxies are not used in weak lensing analysis, their identification is vital in order to exclude them from the background galaxy catalogue, avoiding the addition of noise to the lens model.
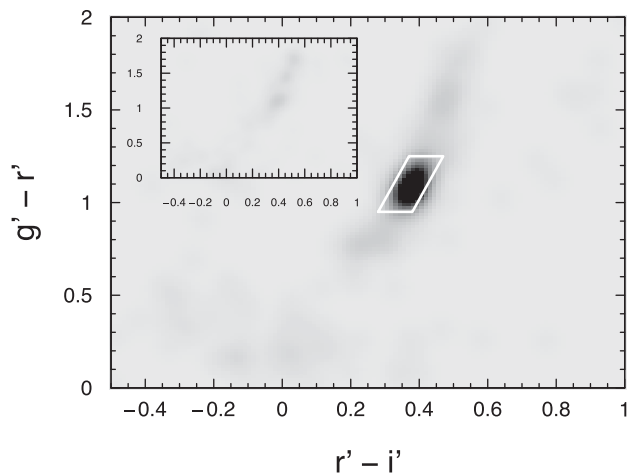
Figure 2. The CC diagram of the galaxies located inside the central (magenta) box of the Fig. 1 and with $r' \leq 19.5$. The evident density peak is related to the red cluster member galaxies. The inset panel shows the same plot for the galaxies located inside the two distant (black) boxes of the same figure. In both plots the linear grey-scale are the same. The white polygon corresponds to the red cluster member locus.

The red cluster members have homogeneous photometric properties, occupying a well-defined *locus* in the colour–colour (CC) diagram (e.g. Medezinski et al. 2010). We have used the $r' - i'$ versus $g' - r'$ diagram then to determine this locus through statistical subtraction. To this purpose, we have considered two different regions: a central one (*magenta* dashed box in Fig. 1), where we expect most cluster members to be, and two distant regions (*black* dashed boxes) where the cluster galaxy counts are negligible compared to the field. We found that the galaxy counts in the central region are higher than those in the distant regions up to $r' = 19.5$. We will therefore take this limit for the cluster member detection.

In Fig. 2, we show the CC diagrams of central and peripheral regions (inset) of the image (Fig. 1). The former presents a clear excess over the latter that is related to the cluster members. By subtracting the number densities in a grid over the CC space, this excess becomes even more evident and thus we define the region marked in the diagram around it. After this process, we have selected 294 members within $r' \leq 19.5$. Their numerical density distribution weighted by the r'-luminosity can be seen in the Fig. 3.

The numerical density distribution weighted by the r'-luminosity shows a trimodal behaviour being the most pronounced feature related to the merging subclusters A3376W and A3376E. At the north, as was previously suggested by Ramella et al. (2007), we have found a sample of galaxies whose colours are compatible with the main A3376 system. The final confirmation about its pertinence or not to A3376 will come from the analysis of the galaxy redshifts in this region. (Section 3).

2.4 Shape measurements

Finding precise corrections for the point spread function (PSF) is a crucial task for the success of shape measurements of faint objects. Specially so in large cameras as DECAM, the PSF exhibits large variation across the field, which has to be taken into account. We mapped the PSF independently on each 44×41 arcmin frame (#1:9 in Fig. 1) by selecting bright, unsaturated stars. Being point-like objects, all deviation from circularity detected in their shapes are due only to instrumental/atmospheric distortion of the PSF. For
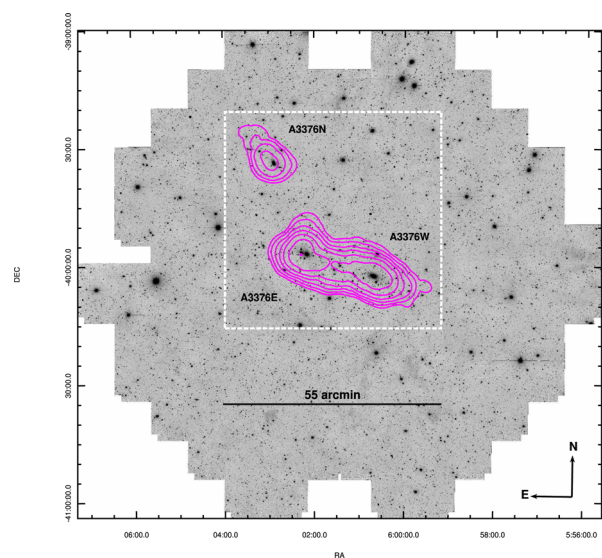

Figure 3. The magenta contours correspond to the numerical density distribution weighted by the r' luminosity for the 294 red sequence galaxies selected through CC statistical subtraction. The 'new' structure A3376N is centred on a bright red luminous galaxy (hereafter BCG N) ~25 arcmin (~1.4 Mpc) apart from the nearest BCG E. The white dashed box delimits the area where we will carry further studies on the mass distribution.

DECAM, the PSF is also magnitude dependent ('the brighter, the fatter'; e.g Melchior et al. 2015) reflecting the tenuous flux variance on the efficiency of the registration charges in the CCD (Antilogus et al. 2014).

Shape measurements of PSF distortion across the field were made with a Bayesian publicly available code IM2SHAPE (Bridle et al. 1998)[2]. This code works by modelling galaxies as a sum of Gaussians with an elliptical basis. On the other hand, stars are modelled as a single Gaussian profile and no deconvolution is performed to keep the PSF parameters, which are the ellipticity components (e_1, e_2), and the FWHM. We have used the R (R Core Team 2014) function thin plate spline regression (TPS; Nychka, Furrer & Sain 2014) to spatially interpolate the discrete set of PSF parameters allowing the model to consider also the corresponding magnitudes. For the sake of quality, we iterated this process three times, each time removing the 10 per cent of objects with the largest absolute residuals[3].

The final measured ellipticities and the corresponding residuals after the spatial and flux interpolation are shown in Fig. 4. In the end, all galaxies were modelled as a sum of two Gaussians with an identical basis and the local was PSF deconvolved. Furthermore, we removed galaxies with large ellipticity errors ($\sigma_e > 2$) and with evidence of contamination by nearby objects.

2.5 Source selection

The shape deformation on background galaxies is used to infer the mass distribution that acted as a gravitational lens. In this sense, it is strictly necessary to perform a careful selection of background galaxies in order to diminish the contamination by both foreground and cluster member galaxies. Because of its proximity ($\bar{z} = 0.046$),
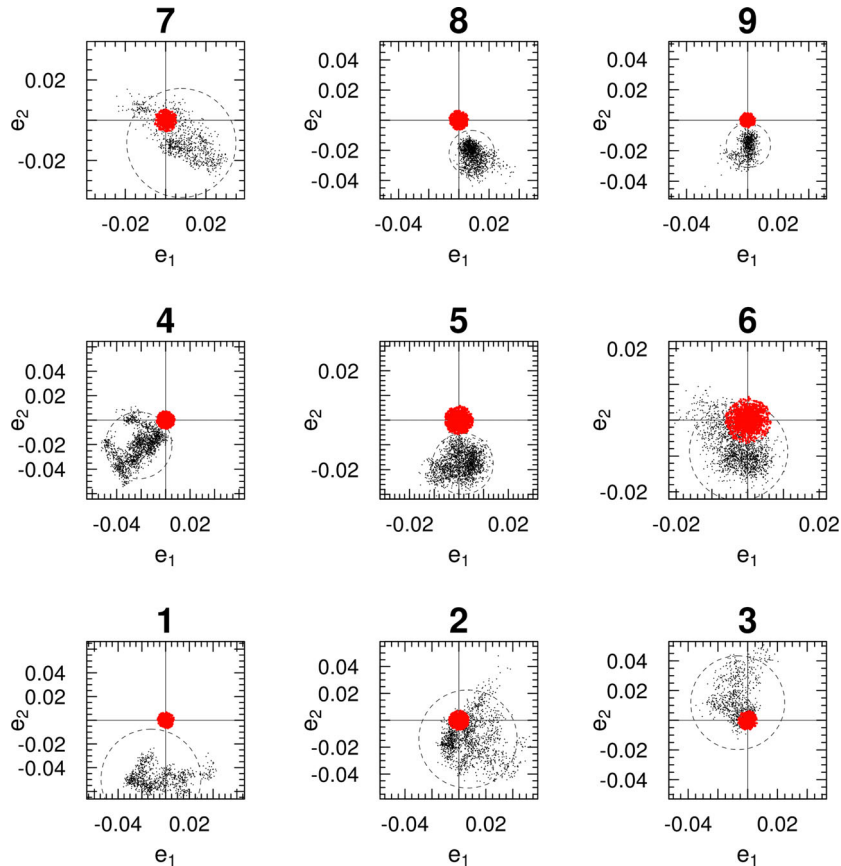
Figure 4. Raw distribution of the ellipticity in Cartesian components e_1 and e_2 measured on selected unsaturated bright stars by IM2SHAPE (black points). Aiming at an accurate PSF correction, we have performed our analysis individually for each frame as defined in Fig. 1. After the iterative process to quantify the PSF effect was finished, we computed the residuals between the model and the data. As shown by the red points, they have good concordance with zero regardless of the initial data spread. The dashed circles comprise 95 per cent of the data.

it is expected that the galaxy sample in the A3376 field is strongly dominated by background ones. For a comparison, the Canada–France–Hawaii Telescope Legacy Survey (CFHTLS)[4], shows that only 0.14 per cent of its galaxies have $z \leq 0.046$, making the contamination by these galaxies negligible. Thus, we have just excluded the red sequence CC locus and considered as background candidates all galaxies having $r' \geq 21$.

Due to the fact that A3376 is located at very low redshift, it is expected that the background structures will appear in the mass map with, at least, comparable or higher signal than the subject galaxy cluster, according to equation (3). In order to overcome this challenging, but unavoidable obstacle, we have concentrated our efforts in extracting the lensing signal of A3376 by reducing the signal coming from high-redshift structures. Without a photometric redshift catalogue for our images, we tested several cut limits for the fainter galaxies (closely related to high-redshift ones) aiming to maximize the signal to noise near the BCG location.

For this purpose, we referred to the mass aperture statistic (Schneider 1996) whose S/N is averaged through the measured tangential ellipticity e_+ for the N_{θ_0} galaxies inside a radius θ_0,

$$\text{S/N} = \frac{\sqrt{2}}{\sigma_e^2} \frac{\sum_{i=1}^{N_{\theta_0}} e_{+_i}(\theta_i) Q_{\text{NFW}}(\theta_i, \theta_0)}{\left[\sum_{i=1}^{N_{\theta_0}} Q_{\text{NFW}}^2(\theta_i, \theta_0)\right]^{1/2}}, \tag{5}$$

where θ_i is the galaxy position and σ_e is the quadratic sum of the measured error and the intrinsic ellipticity uncertainty, estimated as 0.35 for our data. The NFW filter (Schirmer 2004),

$$Q_{\text{NFW}}(\theta_i, \theta_0) = [1 + e^{a-b\chi(\theta_i, \theta_0)} + e^{-c+d\chi(\theta_i, \theta_0)}]^{-1}$$
$$\times \frac{\tanh[\chi(\theta_i, \theta_0)/\chi_c]}{\pi \theta_0^2 [\chi(\theta_i, \theta_0)/\chi_c]}, \tag{6}$$

where $\chi = \theta_i/\theta_0$, describes approximately the NFW shear profile. Hetterscheidt et al. (2005) suggest, as optimized parameters for the halo detection maximization, $a = 6$, $b = 150$, $c = 47$, $d = 50$, $\chi_c = 0.15$ and $\theta_0 = 11$ arcmin.

The S/N map of the central region (*white* box in Fig. 3) is presented in Fig. 5. As expected, it shows a multistructure scenario. The highest S/N peaks around the BGCs are reported by the $21 \leq r' \leq 24.5$ limited sample, hereafter our fiducial background sample. This final background sample had a field density of 12.3 galaxies per arcmin^{-2}. The comparison with CFHTLS allowed us to estimate the critical density as $\Sigma_{\text{cr}} = 9.6 \times 10^9$ M$_\odot$ kpc^{-2}.

2.6 Mass reconstruction

Now, from measured ellipticities, we reconstructed the mass distribution using the code LENSENT2 (Marshall et al. 2002). Its Bayesian method is based on the maximum entropy algorithm (Seitz, Schneider & Bartelmann 1998), which works to minimize a χ^2-like
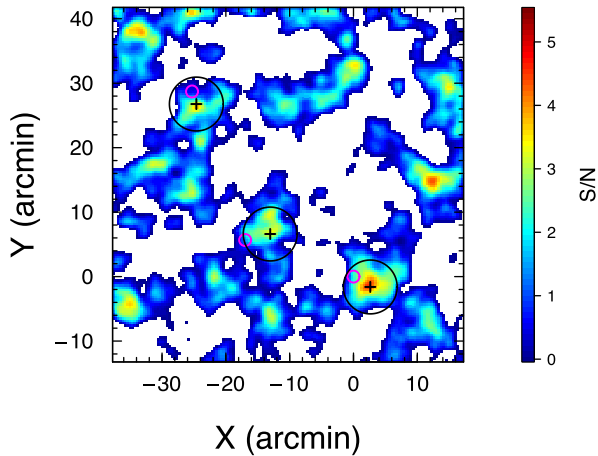
Figure 5. Signal-to-noise map obtained through the mass aperture statistic (Schneider 1996) considering a fainter limit of $r_{max} = 24.5$. The white regions correspond to a negative S/N. The BCGs are marked as small magenta circles whereas their neighbouring highest S/N peaks ('+') are marked as large black circles. Because of the low redshift, A3376 is surrounded by a lot of background structures.

statistics based on the comparison between the measured ellipticity field with those the model predicts. The field is smoothed by a Gaussian filter with $\sigma = 160$ arcsec that was the best compromise between the signal to noise in the final map. This smoothing is required since each galaxy is not isolated, i.e. they are correlated with those in their neighbourhoods.

The resulting mass distribution is presented in Fig. 6. The mass structures of subclusters were identified as the closest to their respective BCGs, as suggested by the previous numerical density distribution weighted by the r'-luminosity (Fig. 3). As anticipated by the S/N map, the mass distribution shows, beyond the (at least) three A3376 related peaks, a great amount of clumps in the field. Moreover, the A3376E subcluster mass distribution looks blended with another nearby mass concentration. In the following, we apply a method to quantify the mass of separate structures and estimate their central position errors.

2.7 Mass distribution modelling

The multipeaked mass distribution brings an additional difficulty to measure the mass of the structures we are interested in. Initial efforts to fit three different NFW profiles for the A3376 related
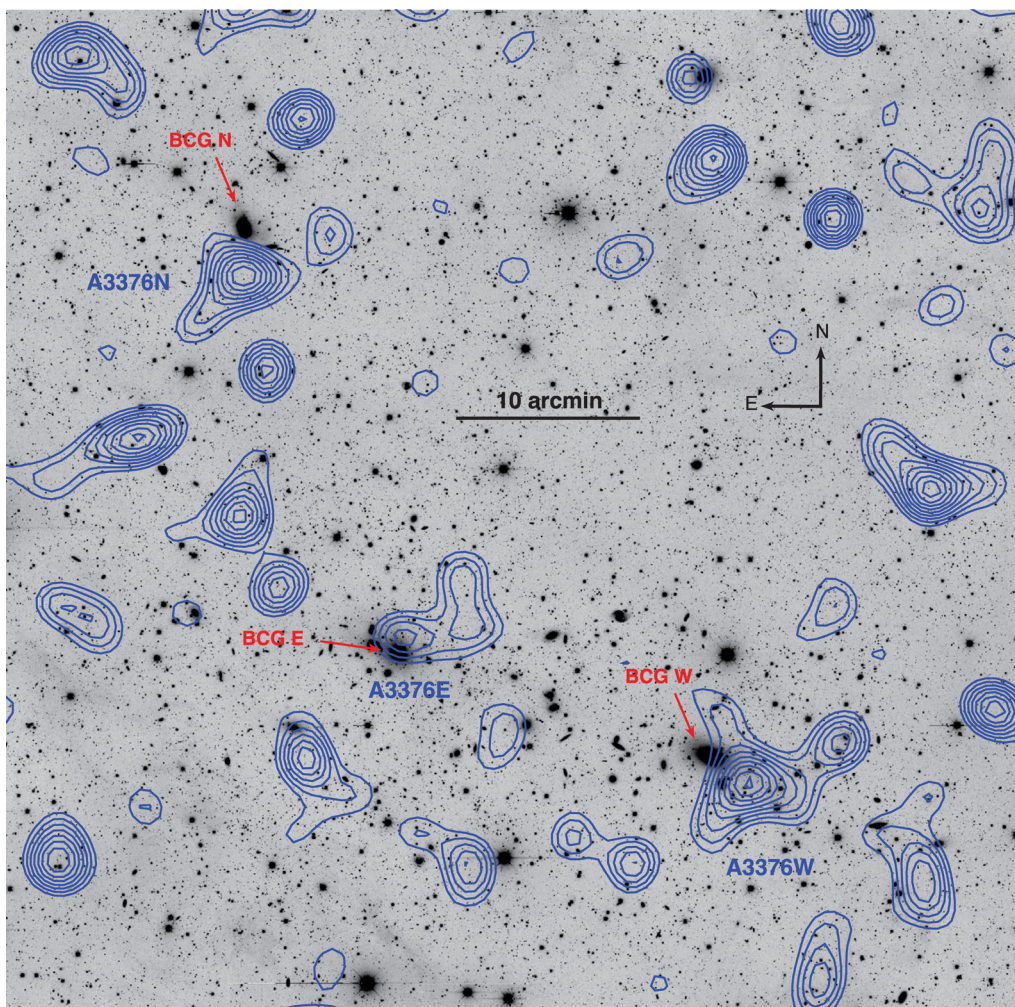

Figure 6. Mass distribution (blue contours) in the central part of A3376 field as obtained by LENSENT2 overlaid with the r'-band image. The contours are linearly spaced by 0.01 within the interval $\kappa \in [0.05: 0.15]$. The merging subclusters A3376W and A3376E were identified as the nearest mass peaks respective to their BCGs. The same procedure was applied to identify the mass concentration related to the northern subcluster candidate A3376N.
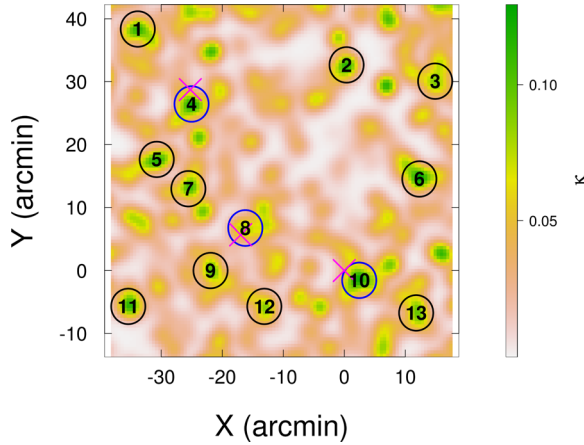
Figure 7. Convergence map showing the most significant mass peaks in A3376 field according to our peak finder method. The circular moving window with $R = 2.8$ arcmin found 13 mass peaks above the minimum significance level 1.6σ, as seen in the A3376E mass related clump. The BCGs are marked with the magenta 'X'. The peaks #10, #8 and #4 correspond, respectively, to the A3376W, A3376E and A3376N subclusters. Our forthcoming model will consider these thirteen peaks simultaneously.

clumps have proven unfruitful because the model did not reach convergence even after many iterations ($\sim 1 \times 10^5$). To properly address this, we had to identify the most relevant structures in the field and then add them into our model.

We searched for peaks inside a moving circular window 2.8 arcmin in radius. This procedure allowed us to identify two subclusters with significances larger than 3σ. As a lower limit, we considered the significance of the A3376E mass concentration (1.6σ). The resulting 13 identified peaks are shown in Fig. 7.

Our fiducial model consists of 13 NFW profiles fitted simultaneously, each one with masses as their unique unknown parameters. In the absence of circular symmetry, we worked with Cartesian components of the effective shear rather than the usual tangential component. The transformation can be done easily just by multiplying g_+ by the lensing convolution kernel.

$$D_1 = \frac{y^2 - x^2}{x^2 + y^2} \quad \text{and} \quad D_2 = \frac{2xy}{x^2 + y^2}, \quad (7)$$

where x and y are the Cartesian coordinates relative to the respective lens centre.

The halo concentration was fixed based on the Duffy et al. (2008) mass–concentration relationship,

$$c = 5.71 \left(\frac{M_{200}}{2 \times 10^{12} \, h^{-1} \, M_{\odot}} \right)^{-0.084} (1 + z)^{-0.47}, \quad (8)$$

where the redshift was considered the same for all haloes[5].

The total effective shear component in each lens position can be written as a contribution of each halo,

$$g_i = \sum_{k=1}^{13} g_i^k, \quad i \in \{1, 2\}. \quad (9)$$

Table 2. Median and 68 per cent range of the marginalized masses in sampled in the MCMC chains.

Subcluster	M_{200} $(10^{14} \, M_{\odot})$
A3376W	$3.0^{+1.3}_{-1.7}$
A3376E	$0.9^{+0.5}_{-0.8}$
A3376N	$1.4^{+0.7}_{-1.0}$

which was compared to the measured ellipticities e_1 and e_2 through the χ^2,

$$\chi^2 = \sum_{j=1}^{N_{\text{sources}}} \sum_{i=1}^{2} \frac{(g_i - e_{i,j})^2}{\sigma_{\text{int}}^2 + \sigma_{\text{obs}_{i,j}}^2}, \quad (10)$$

where $\sigma_{\text{obs}_{i,j}}$ corresponds to errors reported by IM2SHAPE, and σ_{int} is the uncertainty associated with the sources intrinsic ellipticity distribution, estimated as 0.35.

In our Bayesian model, the posterior of the problem is given by

$$\Pr(M|\text{data}) \propto \mathcal{L}(\text{data}|M) \times \mathcal{P}(M), \quad (11)$$

where, additionally, we adopted a uniform prior $0 < M \leq 8 \times 10^{15} \, M_{\odot}$ to allow the chains to quickly reach the stationary state. Considering the data normally distributed around the model, we can associate the likelihood with the previous χ^2 statistics as

$$\ln \mathcal{L} \propto -\frac{\chi^2}{2}. \quad (12)$$

2.8 Results

We evaluated the posterior described in equation (11) by using an MCMC (Monte Carlo Markov chain) algorithm with a simple Metropolis sampler implemented in the R package MCMCMETROP1R (Martin, Quinn & Park 2011). We generate four chains of 1×10^5 points allowing an additional 1×10^4 points first as 'burn-in' to ensure the chains fully represent the stationary state. The potential scale factor R, as implemented in the CODA package (Plummer et al. 2006), has shown that the final combined chain is, within 68 per cent c.l., convergent ($R < 1.05$).

Subcluster masses, marginalized over all parameters, are presented in Table 2. For the merging system, we have obtained $M_{200}^{\text{W}} = 3.0^{+1.3}_{-1.7} \times 10^{14} \, M_{\odot}$ and $M_{200}^{\text{E}} = 0.9^{+0.5}_{-0.8} \times 10^{14} \, M_{\odot}$. This corresponds to a total mass $M_{200}^{\text{W+E}} = 4.1^{+1.5}_{-1.8} \times 10^{14} \, M_{\odot}$. We have found that the probability of A3376E being the most massive one is of only 9 per cent. For A3376N, we obtained $M_{200}^{\text{N}} = 1.4^{+0.7}_{-1.0} \times 10^{14} \, M_{\odot}$.

We can now ask about the relative position of the mass and X-ray distributions. We have used publicly available *XMM–Newton* observations of A3376 made in 2003 (Obs Id. 0151900101; PI M. Markevitch) and 2007 (Obs Id. 0504140101; P.I. M. Johnston-Hollitt). We have previously used these observations in Machado & Lima Neto (2013) in order to constrain the dynamical modelling of A3376.

For completeness, we summarize here the procedure we have used to make the X-ray intensity map with the EPIC camera data. The *XMM–Newton* data were processed through the SAS[6] pipeline, following the procedure recommended in their site, and keeping only events in the field of view with PATTERN $\leq$ 12 (MOS 1 and 2) and PATTERN $\leq$ 4 (pn). Finally, we have used light curves in

---

[5] We have considered all of them located at the A3376 redshift.

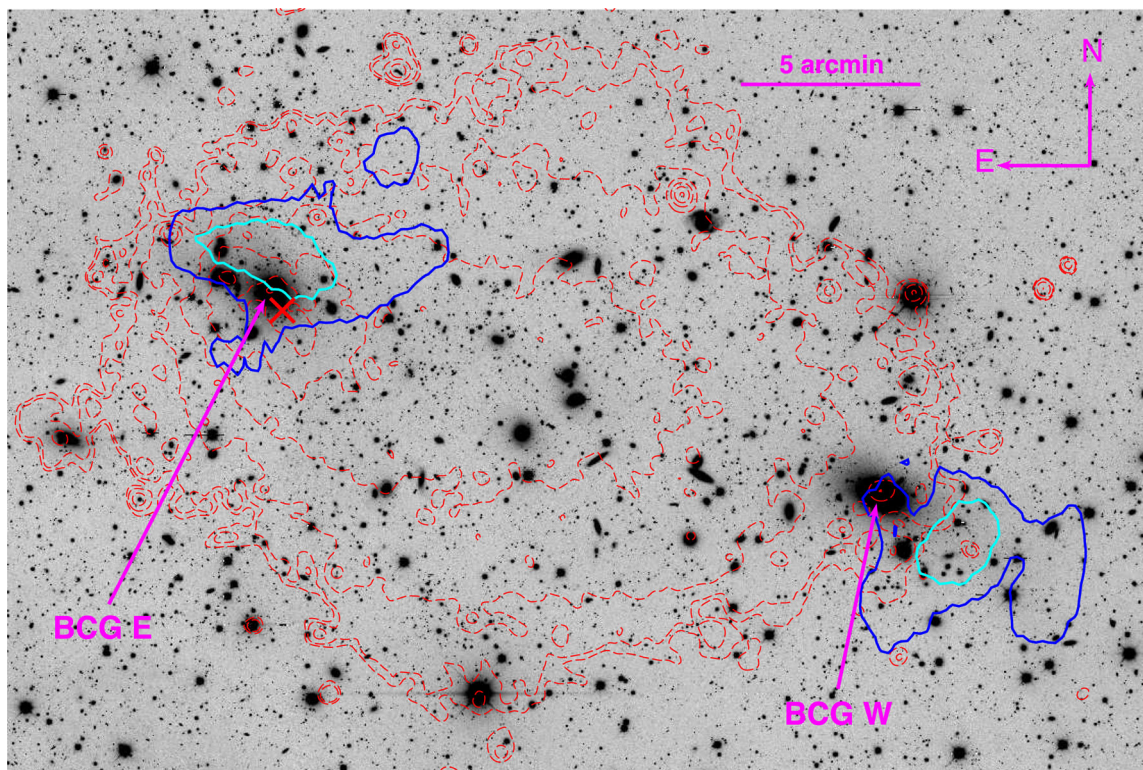[6] Science Analysis System 11, http://xmm.esac.esa.int/

Figure 8. Optical *r'* band overlaid with *XMM–Newton* X-ray contours (red dashed lines) and the confidence contours of 68 per cent c.l. (cyan) and 95 per cent c.l. (blue) of the mass centre positions. The X-ray distribution is unimodal (the red 'X' marks it peak) with the peak related to the A3376E subcluster. Both BCG and X-ray position are comparable within 95 per cent c.l. with the mass centre. The same BCG behaviour in relation to the mass centre is reported on A3376W.

order to exclude high particle background time intervals from the observations. With the cleaned event files, we have made exposure map corrected images in broad-band (0.5–8.0 keV) and then combined all images (from both observations and for all EPIC cameras) into a single intensity map mosaic.

The multipeaked field prevents the simultaneous centre position and mass modelling (e.g. Monteiro-Oliveira et al. 2017). To estimate the uncertainties on the mass centre positions, we performed 1×10^4 bootstrap re-samplings of the ellipticity field. For each one, we have reconstructed the mass distribution (as described in Section 2.6) and mapped the position of the nearest peak in relation to those previously identified (Fig. 7). The confidence contours are presented in Fig. 8.

The comet-like X-ray morphology reveals just one more concentrated location close to the BCG E. Their positions are, within 95 per cent c.l., in agreement to both BCG and mass centre location. On the other hand, the subcluster A3376W seems to have had its gas stripped-off during the collision. According to the simulations of Machado & Lima Neto (2013), this feature could be understood as the result of a collision between two haloes having different central gas concentrations. In that scenario, the smaller subcluster A3376E is the more concentrated one. It is able to retain its gaseous core after the collision.

3 DYNAMICAL ANALYSIS

3.1 Spectroscopic data

A subsequent search on *NASA Extragalactic Database* (NED) revealed 239 galaxies with available redshifts in the A3376 DECAM field. In these galaxies, 173 were spectroscopic members after implementing a 3σ-clipping procedure (Yahil & Vidal 1977). Their spatial distribution, seen in Fig. 9, follow closely the photometric red sequence distribution (Fig. 3). Their respective redshift distribution is shown in Fig. 10. For the analysis, we considered only the densest regions, selecting the galaxies located inside the *yellow* circles in Fig. 9 as the fiducial sample.

3.2 A3376N

The 3σ-clipping applied over the whole galaxy sample has shown that the galaxies associated with the subcluster candidate have redshifts comparable with those found in the main system. The seven identified galaxies have $\bar{z} = 0.0472 \pm 0.0005$ with a velocity dispersion of $\sigma_v/(1 + \bar{z}) = 414 \pm 82$ km s^{-1}.

3.3 A3376W and A3376E

For the merging system, we have selected the innermost galaxies located inside the two circular regions ($R = 18$ arcmin) centred on each BCG. The 132 spectroscopic cluster members have $\bar{z} = 0.0461 \pm 0.0003$ and $\sigma_v/(1 + \bar{z}) = 835 \pm 45$ km s^{-1} being, with 99 per cent c.l., Gaussian distributed (p-value = 0.49 according to the Anderson–Darling test). The Δ-test (Dressler & Shectman 1988) points to the absence of substructures with 99 per cent c.l. (p-value = 0.53; Hou et al. 2012).

We used the *n*-dimensional Gaussian mixture model algorithm implemented in the R package MCLUST (Fraley et al. 2012). The attempt to use the 1D-MCLUST to classify the galaxies according to their respective subcluster was, however, unsuccessful. According
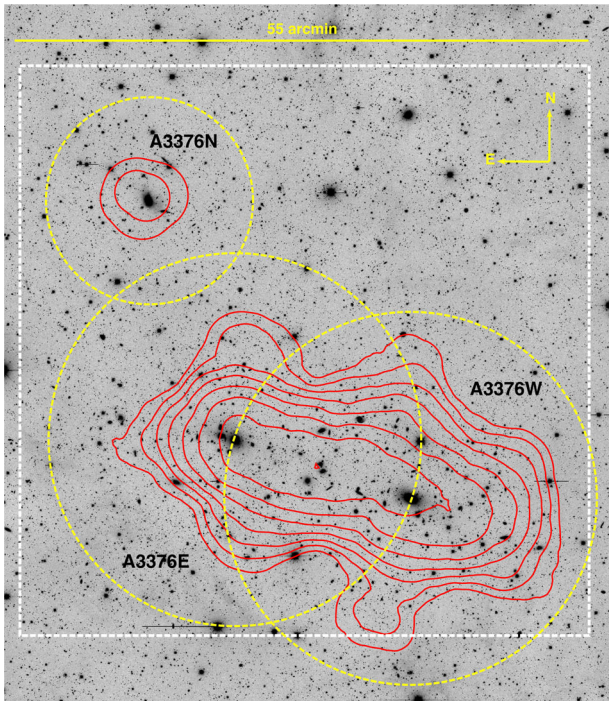
Figure 9. Density logarithm contours (red) of the 173 spectroscopic galaxy members found by the 3σ-clipping procedure (Yahil & Vidal 1977). These galaxies shows good match with the already selected photometric red sequence galaxies. In our analysis, we have considered only the densest regions of the field, highlighted by the yellow circles centred on the respective BCG. For A3376N, we selected galaxies inside an $R \leq 10$ arcmin circle, whereas for A3376W and A3376E the circles had $R = 18$ arcmin. Despite the intersection between A3376N and A3376E, there is no galaxy in this region. The other 31 member galaxies are spread along the field.
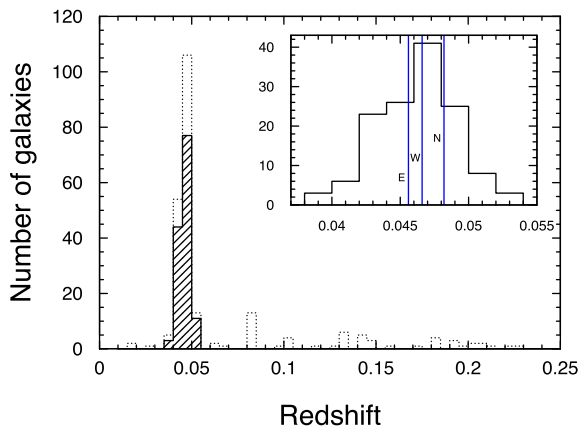

Figure 10. Redshift distribution of the 239 galaxies in A3376 field (dotted lines). The inset panel, corresponding to the hatched histogram, shows the 132 members of the merging system A3376W and A3376E. This sample comprises the galaxies located inside the combined circular regions with $R \leq 18$ arcmin centred on the BCGs W and E selected after the application of the 3σ-clipping. This sample has $\bar{z} = 0.0461 \pm 0.0003$ and $\sigma_v/(1 + \bar{z}) = 835 \pm 45$ km s^{-1}. The vertical lines are showing each BCG redshift. Four galaxies having $z > 0.25$ were omitted for clarity.

to the Bayesian Information Criterion (BIC), the preferred model (a single group) is strongly favoured over the second best model (two groups) with $\Delta\mathrm{BIC} = 8$ (Kass & Raftery 1995). The absence of large substructures in the redshift space is a hint that the merger axis is near to the plane of the sky and/or the system is close to the most distant point in their orbit (e.g. Golovich et al. 2016; Monteiro-Oliveira et al. 2017).

In order to overcome the impossibility of using the redshifts as subcluster proxies, we have turned to the photometric red sequence galaxies. We have added the spectroscopic cluster members that are not initially in the sample for a total of 192 galaxies (70 per cent spectroscopic members). The 2D-MCLUST shows bimodality as the best result, with $\Delta\mathrm{BIC} = 5$ in relation to the second best unimodal distribution. The recovered subclusters, shown in Fig. 11, can be immediately related to the merging subclusters. Both are Gaussian with 99 per cent c.l. and are separated only by $\delta v/(1 + \bar{z}) = 181 \pm 147$ km s^{-1} (68 per cent c.l.) along the line of sight. More details are presented in Table 3.

The results are robust among several covariance matrix parametrizations implemented on MCLUST. We also checked a possible contamination by galaxies belonging to the neighbouring subcluster. We remade the analysis only for the very innermost galaxies ($R \leq 8$ arcmin), and found similar results for the subclusters' mean redshift as well $\delta v/(1 + \bar{z})$.

The attempt to use the combined redshift plus spatial coordinates (3D-MCLUST) was also fruitless to disentangle the subclusters' galaxies ($\Delta\mathrm{BIC} = 2.4$ relative to the second best bimodal solution). However, by setting $k = 2$ groups, the algorithm brings the same result as its two-dimensional version.

4 MERGER DYNAMICS

4.1 A3376W and A3376E

Our previous mass reconstruction and dynamical analysis enabled us to characterize the merger only at the observed time. In order to recover the A3376 merger history, we have applied the MONTE CARLO MERGER ANALYSIS CODE (MCMAC; Dawson 2013). This model presents an improvement with respect to the famous time argument model (Beers, Geller & Huchra 1982), because it provides the covariance estimation of the involved parameters (e.g. velocity, age and separation). The MCMAC considers a binary collision between two truncated NFW profiles. The input parameters, listed on Table 4, were resampled through 2.5×10^5 realizations and applied to the model afterwards.

Normally, MCMAC considers the merger direction equally probable between $0°$ and $90°$ from the plane of the sky. However, we have sufficient elements to better constrain this value. The two subclusters are separated in line of sightby 181 ± 147 km s^{-1}. Concomitantly, the perpendicular velocity can be evaluated from the estimated shock velocity ($v_{\mathrm{shock}} < 2000$ km s^{-1}; Akamatsu et al. 2012). Springel & Farrar (2007) and more recently Machado et al. (2015) have shown that halo velocity corresponds only to a fraction of the shock propagation. Considering 1000 ± 500 km s^{-1} as the halo propagation velocity, we found a merger axis located at $\alpha = 11° \pm 10°$ with respect to the plane of the sky. Conservatively, we have adopted a prior in MCMAC, allowing α to assume any value between $0°$ and $20°$ with equal probability.

The MCMAC results are shown in Table 5. For comparison, the prior applied on α reduced by $\sim$58 per cent the error bar on the merger age (TSC_0) in relation to the unconstrained input.
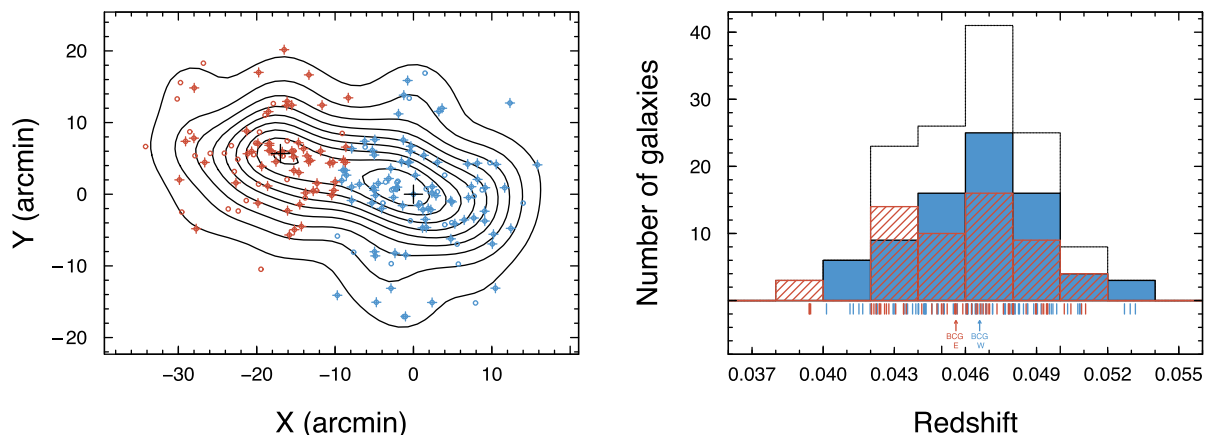
Figure 11. 2D-MCLUST results. Left: spatial distribution of the subclusters A3376W (blue) and A3376E (red) overlaid with the linear density contours for the 192 selected galaxies (continuous black lines). The '+' denotes the galaxies with available redshift, the black ones being the BCGs. Right: total redshift distribution (black lines) overlaid with the recovered subclusters distribution following the same previous colour scheme. According to the Anderson–Darling test, both groups follow Gaussian distributions with 99 per cent c.l. Their line-of-sight separation is only $\delta v/(1 + \bar{z}) = 181 \pm 147$ km s^{-1}.

Table 3. Dynamics of the subclusters A3376W and A3376E modelled by 2D-MCLUST.

	A3376W	A3376E
Number of galaxies	79	56
$\bar{z}$	0.0464 ± 0.0003	0.0458 ± 0.0004
$\sigma_v/(1 + \bar{z})$ (km s^{-1})	815 ± 60	858 ± 66

Table 4. The MCMAC input parameters based on our previous analysis. From the redshifts, we can estimate the current relative radial velocity of the subclusters, $v_{\rm rad}(t_{\rm obs})$ (for more details see Dawson 2013). The projected distance $d_{\rm proj}$ corresponds to the mass peak separation.

Parameter	Value	Uncertainty	Unit
M^W_{200}	3.0	1.7	10^{14} M$_\odot$
M^E_{200}	0.9	0.8	10^{14} M$_\odot$
z_W	0.0464	0.0003	–
z_E	0.0458	0.0004	–
$d_{\rm proj}$	1096	66	kpc

Table 5. The MCMAC parameter estimation related to A3376W and A3376E merger. The first three lines show the input quantities: α is the merger direction in relation to the plane of the sky, $d_{3D}(t_{\rm obs}) = d_{\rm proj}/\cos\alpha$ is the current 3D distance between the subclusters and $v_{3D}(t_{\rm obs}) = v_{\rm rad}(t_{\rm obs})/\sin\alpha$ is the current 3D relative velocity. The following lines present the quantities calculated by the model: $d_{3D_{\max}}$ is the 3-D maximum subcluster separation; $v_{3D}(t_{\rm col})$ is the 3-D velocity at collision time; $v_{3D_{\max}}$ is the maximum relative velocity; TSC$_0$ is the time since collision for the outgoing scenario; TSC$_1$ is the time since collision for the incoming scenario and T is the collision period.

Parameter	Unit	Median	68 per cent c.l.
α	$^\circ$	11	8–19
$d_{3D}(t_{\rm obs})$	Mpc	1.1	1.0–1.2
$v_{3D}(t_{\rm obs})$	km s^{-1}	717	0–991
$d_{3D_{\max}}$	Mpc	1.4	1.0–1.9
$v_{3D}(t_{\rm col})$	km s^{-1}	1878	1581–2121
$v_{3D_{\max}}$	km s^{-1}	2477	2175–2829
TSC$_0$	Gyr	0.9	0.6–1.1
TSC$_1$	Gyr	2.5	1.1–3.2
T	Gyr	3.5	2.2–4.1

In the outgoing scenario, A3376W&E are currently seen $0.9^{+0.2}_{-0.3}$ Gyr after the pericentric passage. This value is comparable, at 99 per cent c.l., with those previously estimated by Akamatsu et al. (2012), Machado & Lima Neto (2013) and George et al. (2015). The collision velocity was 1878^{+243}_{-297} km s^{-1}, having been reduced to 717^{+274}_{-717} km s^{-1} at the observation time. According to their relative position, the subclusters are nearly close to the apoapsis, 1.4 ± 0.4 Mpc, given their current separation of 1.1 ± 0.1 Mpc.

As an alternative scenario, we considered one in which the subclusters are returning after reaching maximum separation. The system is then seen $2.5^{+0.7}_{-1.4}$ Gyr after the collision. In the MCMAC sampling, TSC$_1$ is less than the age of the universe at the cluster redshift in ∼90 per cent of the realizations, in the sense that using only these results, we cannot discard the incoming scenario.

The model degeneracy can be broken by comparing each scenario prediction with an observational feature. One of the remarkable features in A3376 are the radio relics found in the outskirts of the system, which are thought to trace current shock positions. In relation to the mass centre of the system, the current shock position can be written as (Ng et al. 2015),

$$s_i = \frac{M_j}{M_i + M_j}\, TSC\, v_{\rm shock}, \qquad (13)$$

where i, j refer to the two subclusters, M is the mass, TSC is either outgoing or incoming age and $v_{\rm shock}$ is the shock velocity propagation. For this, we have chosen a uniform distribution $\mathcal{U}(1600$–2600 km s$^{-1})$ taking into account both observational (Akamatsu et al. 2012) and numerical (Machado & Lima Neto 2013) estimates. The resulting expected shock positions are shown in Fig. 12.

Both relic positions argue in favour of the outgoing scenario. If the conclusion is not readily obvious in the W shock, where the models are compatible with 68 per cent confidence level, it is made explicit in the east shock: the outgoing scenario is ∼12 times more probable than the alternative one.

4.2 A3376E and A3376N

Although there is no observation of the ICM in the subcluster A3376N, we can conjecture about the interaction between it and the colliding system. A complete approach requires a complete
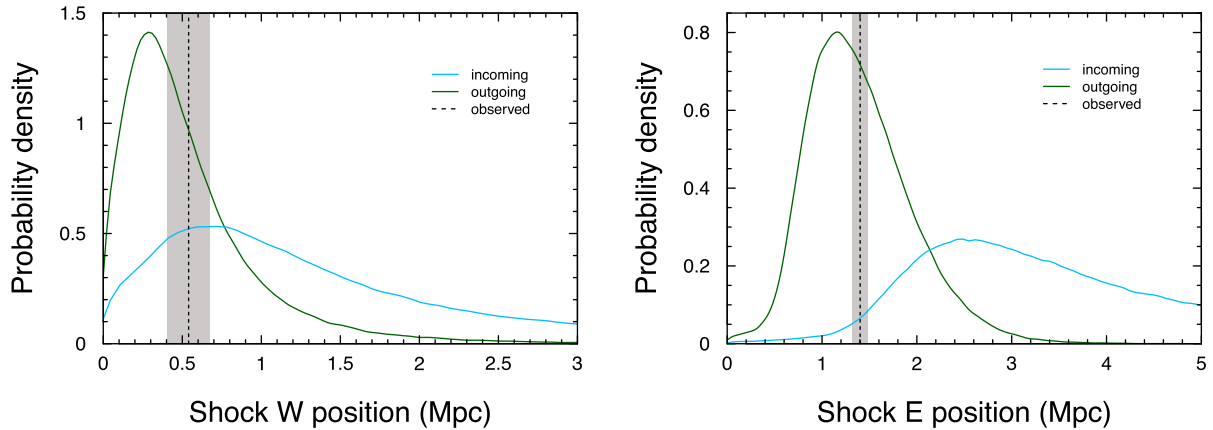
Figure 12. Predicted radio relics positions with respect to the system mass centre calculated from the outputs of the two-body model. The outgoing and incoming posteriors are, respectively, the green and cyan lines. The measured relic position corresponds to the dashed line where we highlighted in *grey* the interval of 68 per cent c.l., considered as the half of each relic width. While both outgoing and incoming scenarios are consistent within 68 per cent c.l. in the western relics, the analysis of the eastern radio relic has showed that the outgoing scenario is ∼12 times more probable than the other one.

three-body model. This, however, lies beyond the scope of this work.

To study a possible interaction between A3376N and A3376E separated by 1147 ± 62 kpc, a simple two-body only toy model can be adopted. We applied the generalized MCMAC to this effect, which considers a possible unbound scenario (Andrade-Santos et al. 2015). Also, in the absence of any merger angle prior, we have used the default uniform distribution[7].

Our results show that in 34.4 per cent of 2.5×10^5 realizations, the model favours an unbound scenario. In this case, there is a preference for small merger angles, $\alpha = 5° \pm 4°$. Conversely, the bound solutions do not provide a good criterion to disentangle the outgoing or incoming scenario. In 34 per cent of the bound resulting realizations, $TSC_1 = 4.8^{+2.0}_{-3.1}$ Gyr is greater than the Universe age at the cluster redshift. For the outgoing configuration, the collision happened 1.5 ± 1.0 Gyr ago with 1849^{-226}_{+234} km s^{-1}. In the apoapsis, the subclusters will then be separated by $2.7^{+1.4}_{-1.6}$ Mpc.

5 DISCUSSION

5.1 A3376N

Both luminosity-weighted density distribution and projected density maps point towards the presence of an additional structure in A3376 field, as suggested by Ramella et al. (2007). Our dynamical analysis confirmed their compatibility with the main A3376 cluster. It is located at $\bar{z} = 0.0472 \pm 0.0005$ having $\sigma/(1 + \bar{z}) = 414 \pm 82$ km s^{-1} and we report a mass of $1.4^{-1.0}_{+0.7} \times 10^{14}$ M$_\odot$. We, however, must still be cautious, as A3376N is undersampled since these conclusions are based on just seven galaxies.

The absence of X-rays observation of its ICM hinder further detailed analysis of possible interactions between A3376N and A3376W&E.

5.2 Merger between A3376W and A3376E

The A3376 redshift makes its weak lensing signal inescapably low. Therefore, background structures will appear that will have compa-
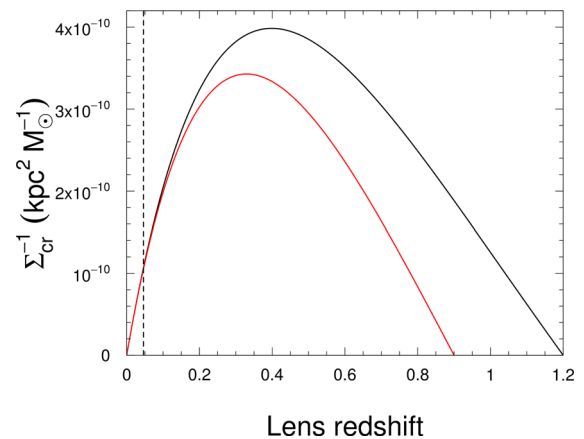
---

[7] A possible merger between A3376E and A3376N does not necessarily follow the same merger direction of the system A3376W and A3376E.

Figure 13. Inverse of the critical surface density Σ_{cr}^{-1} as a function of the lens redshift . The black line represents the case in which the background sources are fixed in $z_{back} = 1.2$ whereas in the red line the same galaxies are the closest, in $z_{back} = 0.9$. While the weak lensing signal ($\propto \Sigma_{cr}^{-1}$) remains nearly the same for a lens located at the A3376 redshift ($\bar{z} = 0.046$, dotted line), the cut of higher redshift sources acts to reduce the signal of higher redshift lenses. In the absence of photometric redshifts, we tried to achieve the goal of removing the higher redshifts lenses by cutting the fainter sources, most of them related to higher redshift.

rable or even higher S/N in the plane of the sky. Aiming to minimize this effect, we manipulated the cutoff for background sample at the faint end, eliminating the most distant galaxies. In Fig. 13, we can see an illustrative example of how the lensing signal changes when we move the background source cut from $z = 1.2$ to $z = 0.9$: while the signal of a lens at $z = 0.046$ does not change, it is diminished for more distant lenses ($z > 0.2$).

It is known that after galaxy cluster mergers, the BCGs will not be at rest with respect to the potential well (generally coinciding with the centre of mass; Guo et al. 2015). This may, at least for some time, violate the central galaxy paradigm (CGP; van den Bosch et al. 2005) that could explain the apparent separation between the Northern BCG and its respective mass peak. However, Guo et al. (2015) have shown that this deviation, in general, is more easily detected in velocity space than in real space. This corroborates our criteria to identify correlated mass concentrations as those closest to the BCGs.

The total mass of the system is $4.1^{+1.5}_{-1.8} \times 10^{14}$ M$_\odot$. This value is, at 68 per cent c.l., in agreement with those estimated by Girardi et al. (1998), based on the galaxy velocity dispersion. The subcluster's masses are $M^W_{200} = 3.0^{+1.3}_{-1.7} \times 10^{14}$ M$_\odot$ and $M^E_{200} = 0.9^{+0.5}_{-0.8} \times 10^{14}$ M$_\odot$, with probability of 91 per cent for A3376W to be the more massive one, as predicted by Machado & Lima Neto (2013).

The X-ray morphology reveals only one peak. The location of this X-ray peak coincides with the locations of both the eastern BCG and of the corresponding mass peak with 95 per cent c.l. On the other hand, A3376W seems to have had its gas mostly stripped off. We have a configuration where one the two mass peaks does not coincide with a peak of X-ray emission. This makes A3376 a dissociative system. It is noteworthy that the most massive structure had its gas content dissipated, whereas the least massive one did not. One possible explanation is the scenario put forth by Machado & Lima Neto (2013), in which the gaseous content of the eastern subcluster is initially four times more concentrated than in the western one. The smaller and denser A3376E passes through the more massive subcluster, disrupting its core. Although A3376W has its gas stripped, A3376E is able to preserve its denser gaseous core, as it emerges from the collision. That simulated scenario had arisen in an attempt to satisfy the observational constraints available then. Now, with the results of the present weak lensing analysis, additional evidence is presented in its favour. The current results confirm that the most important mass peak is indeed found towards the tail of the cometary shape, and not near the location of the X-ray peak.

Our dynamical analysis found that the subclusters are very close in the direction of the line of sight. The separation is only $\delta_v/(1+\bar{z}) = 181 \pm 147$ km s^{-1} which, combined with the estimated perpendicular velocity, yields a small merger angle of $10° \pm 11°$. According to the two-body dynamical model, A3376W&E are seen ~0.8 Gyr after the pericentric passage. This value is consistent with previous estimations based on the shock position (Akamatsu et al. 2012), hydrodynamical simulations (Machado & Lima Neto 2013) and the study of the radio relics (George et al. 2015). Despite the mass error bars being large, tests have shown that if we reduced them by 90 per cent, this would not bring significant differences on the estimated age. The more restrictive parameter estimation would come from the application of priors based on other observables (e.g. X-ray temperature boost; Dawson 2013).

From the measured masses, we can verify the merger dynamical effect on the galaxy velocity dispersion by comparing their pre-merger values with those measured in the dynamical analysis (Monteiro-Oliveira et al. 2017). From the scaling relations proposed by Biviano et al. (2006), we have found a pre-merger value of 750^{+134}_{-128} km s^{-1} and 505^{+125}_{-121} km s^{-1}, for A3376W and A3376E respectively, under mass conservation during the collision. Defining the velocity dispersion boost factor as $f \equiv \sigma_{obs}/\sigma_{pre}$, we found $f_W = 1.1^{+0.2}_{-0.3}$ and $f_E = 1.7^{+0.4}_{-0.5}$. Since these two values are greater than one, a post-collisional scenario is favoured in both cases (see fig. 29 of Pinkney et al. 1996).

Our general results corroborate the merger scenario previously proposed by Machado & Lima Neto (2013). The weak lensing analysis suggests two mass concentrations around the two BCGs. Based on the two-body dynamical model, we have found that A3376W&E is seen after $0.9^{+0.2}_{-0.3}$ Gyr after the pericentric passage and are currently going to the orbit apoapsis. On the other side, the present work suggests that the merger direction is only $11° \pm 10°$ from the plane of the sky, whereas the previous simulations prefer a value of $40°$.

6 SUMMARY

(i) Our large field-of-view images have enabled us to confirm that A3376 is, actually, a trimodal system. The 'new' structure, located ~1150 kpc north-east from A3376E, has a mass $1.4^{+0.7}_{-1.0} \times 10^{14}$ M$_\odot$. The seven spectroscopic member galaxies show that the structure has a mean redshift of 0.0472 ± 0.0005 and a velocity dispersion of 414 ± 82 km s^{-1}.

(ii) Despite the challenges to the task, posed by the very low redshift of A3376, we have succeeded in determining the mass distributions of merging subclusters. We found the individual masses $M^W_{200} = 3.0^{+1.3}_{-1.7} \times 10^{14}$ M$_\odot$ and $M^E_{200} = 0.9^{+0.5}_{-0.8} \times 10^{14}$ M$_\odot$ leading to a ratio $M_W/M_E = 3.3^{+2.0}_{-3.0}$. Additionally, we found that there is a probability of 91 per cent that A3376W is the most massive subcluster.

(iii) The X-ray morphology presents only one X-ray peak, related to A3376E. It is, with 95 per cent c.l., in agreement with both BCG and mass peak positions. On the other hand, the gas content of A3376W seems to have been stripped out.

(iv) Our cluster member classification based on galaxy spatial distribution plus redshift points out that A3376W&E are located close to each other in relation to the line of sight. The velocity difference is only $\delta_v/(1+\bar{z}) = 181 \pm 147$ km s^{-1}; combined with an estimation of the perpendicular velocity based on the shock propagation, we found that the merger is taking place just at $11° \pm 10°$ from the plane of the sky;

(v) According to the two-body model, the collision occurred $0.9^{+0.2}_{-0.3}$ Gyr ago with a velocity of 1849^{+234}_{-226} km s^{-1}. Notwithstanding the model degeneracy, the radio relic positions support the outgoing scenario.

REFERENCES

Adelman-McCarthy J. K., 2011, VizieR Online Data Catalog, 2306
Akamatsu H., Takizawa M., Nakazawa K., Fukazawa Y., Ishisaki Y., Ohashi T., 2012, PASJ, 64, 67
Andrade-Santos F. et al., 2015, ApJ, 803, 108

Antilogus P., Astier P., Doherty P., Guyonnet A., Regnault N., 2014, J. Instrum., 9, C03048

Bagchi J., Durret F., Neto G. B. L., Paul S., 2006, Science, 314, 791

Beers T. C., Geller M. J., Huchra J. P., 1982, ApJ, 257, 23

Bertin E., Arnouts S., 1996, A&AS, 117, 393

Biviano A., Murante G., Borgani S., Diaferio A., Dolag K., Girardi M., 2006, A&A, 456, 23

Bridle S. L., Hobson M. P., Lasenby A. N., Saunders R., 1998, MNRAS, 299, 895

Cassano R., Ettori S., Giacintucci S., Brunetti G., Markevitch M., Venturi T., Gitti M., 2010, ApJ, 721, L82

Clowe D., Gonzalez A., Markevitch M., 2004, ApJ, 604, 596

Coupon J. et al., 2009, A&A, 500, 981

Dawson W. A., 2013, ApJ, 772, 131

Dressler A., 1980, ApJ, 236, 351

Dressler A., Shectman S. A., 1988, AJ, 95, 985

Duffy A. R., Schaye J., Kay S. T., Dalla Vecchia C., 2008, MNRAS, 390, L64

Durret F., Perrot C., LimaNeto G. B., Adami C., Bertin E., Bagchi J., 2013, A&A, 560, A78

Ebeling H., Voges W., Bohringer H., Edge A. C., Huchra J. P., Briel U. G., 1996, MNRAS, 281, 799

Fasano G. et al., 2006, A&A, 445, 805

Feretti L., Gioia I. M., Giovannini G., eds, 2002, Merging Processes in Galaxy Clusters Astrophysics and Space Science Library Vol. 272.

Flin P., Krywult J., 2006, A&A, 450, 9

Fraley C., Raftery A. E., Scrucca L., Murphy T. B., Fop M., 2012, mclust Version 4 for R: Normal Mixture Modeling for Model-Based Clustering, Classification and Density Estimation. Available at http://CRAN.R-project.org/package=mclust

George L. T. et al., 2015, MNRAS, 451, 4207

Girardi M., Giuricin G., Mardirossian F., Mezzetti M., Boschin W., 1998, ApJ, 505, 74

Golovich N., Dawson W. A., Wittman D., Ogrean G., van Weeren R., Bonafede A., 2016, ApJ, 831, 110

Guo H. et al., 2015, MNRAS, 446, 578

Hetterscheidt M., Erben T., Schneider P., Maoli R., van Waerbeke L., Mellier Y., 2005, A&A, 442, 43

Hou A. et al., 2012, MNRAS, 421, 3594

Kale R., Dwarakanath K. S., Bagchi J., Paul S., 2012, MNRAS, 426, 1204

Kass R. E., Raftery A. E., 1995, J. Am. Stat. Assoc., 90, 773

Machado R. E. G., LimaNeto G. B., 2013, MNRAS, 430, 3249

Machado R. E. G., Monteiro-Oliveira R., LimaNeto G. B., Cypriano E. S., 2015, MNRAS, 451, 3309

Markevitch M., Vikhlinin A., 2007, Phys. Rep., 443, 1

Marshall P. J., Hobson M. P., Gull S. F., Bridle S. L., 2002, MNRAS, 335, 1037

Martin A. D., Quinn K. M., Park J. H., 2011, J. Stat. Softw., 42, 22

Medezinski E., Broadhurst T., Umetsu K., Oguri M., Rephaeli Y., Benítez N., 2010, MNRAS, 405, 257

Melchior P. et al., 2015, MNRAS, 449, 2219

Mellier Y., 1999, ARA&A, 37, 127

Monteiro-Oliveira R., Cypriano E. S., Machado R. E. G., LimaNeto G. B., Ribeiro A. L. B., Sodré L., Dupke R., 2017, MNRAS, 466, 2614

Ng K. Y., Dawson W. A., Wittman D., Jee M. J., Hughes J. P., Menanteau F., Sifón C., 2015, MNRAS, 453, 1531

Nychka D., Furrer R., Sain S., 2014, Fields: Tools for Spatial Data. Available at http://CRAN.R-project.org/package=fields

Parekh V., van der Heyden K., Ferrari C., Angus G., Holwerda B., 2015, A&A, 575, A127

Pinkney J., Roettiger K., Burns J. O., Bird C. M., 1996, ApJS, 104, 1

Plummer M., Best N., Cowles K., Vines K., 2006, R News, 6, 7

R Core Team, 2014, R: A Language and Environment for Statistical Computing. R Foundation for Statistical Computing, Vienna, Austria, available at http://www.R-project.org/

Ramella M. et al., 2007, A&A, 470, 39

Sarazin C. L., 2004, J. Korean Astron. Soc., 37, 433

Schirmer M., 2004, PhD thesis, Rheinischen Friedrich-Wilhelms-Universität Bonn

Schneider P., 1996, MNRAS, 283, 837

Schneider P., 2005, preprint (astro-ph/0509252)

Seitz S., Schneider P., Bartelmann M., 1998, A&A, 337, 325

Spinelli P. F., Seitz S., Lerchster M., Brimioulle F., Finoguenov A., 2012, MNRAS, 420, 1384

Springel V., Farrar G. R., 2007, MNRAS, 380, 911

Struble M. F., Rood H. J., 1999, ApJS, 125, 35

Valdes F., Gruendl R., DES Project, 2014, in Manset N., Forshay P., eds, ASP Conf. Ser. Vol. 485, Astronomical Data Analysis Software and Systems XXIII. Astron. Soc. Pac., San Francisco, p. 379

van den Bosch F. C., Weinmann S. M., Yang X., Mo H. J., Li C., Jing Y. P., 2005, MNRAS, 361, 1203

Yahil A., Vidal N. V., 1977, ApJ, 214, 347

This paper has been typeset from a TEX/LATEX file prepared by the author.